DOI: 10.1002/chem.200700714

A Wheel-Shaped Single-Molecule Magnet of $[Mn^{II}_3Mn^{III}_4]$: Quantum Tunneling of Magnetization under Static and Pulse Magnetic Fields

Satoshi Koizumi,[a] Masayuki Nihei,[a] Takuya Shiga,[a] Motohiro Nakano,[b] Hiroyuki Nojiri,[c] Roland Bircher,[d] Oliver Waldmann,[d] Stefan T. Ochsenbein,[d] Hans U. Güdel,[d] Felix Fernandez-Alonso,[e] and Hiroki Oshio*[a]

Abstract: The reaction of *N*-(2-hydroxy-5-nitrobenzyl)iminodiethanol (= H_3(5-NO_2-hbide)) with $Mn(OAc)_2 \cdot 4H_2O$ in methanol, followed by recrystallization from 1,2-dichloroethane, yielded a wheel-shaped single-molecule magnet (SMM) of $[Mn^{II}_3Mn^{III}_4$(5-NO_2-hbide)$_6]\cdot 5C_2H_4Cl_2$ (**1**). In **1**, seven manganese ions are linked by six tri-anionic ligands and form the wheel in which the two manganese ions on the rim and the one in the center are Mn^{II} and the other four manganese ions are Mn^{III} ions. Powder magnetic susceptibility measurements showed a gradual increase with $\chi_m T$ values as the temperature was lowered, reaching a maximum value of 53.9 emu mol^{-1} K. Analyses of magnetic susceptibility data suggested a spin ground state of $S = 19/2$. The zero-field splitting parameters of D and B^0_4 were estimated to be $-0.283(1)$ K and $-1.64(1)\times 10^{-5}$ K, respectively, by high-field EPR measurements (HF-EPR). The anisotropic parameters agreed with those estimated from magnetization and inelastic neutron scattering experiments. AC magnetic susceptibility measurements showed frequency-dependent in- and out-of-phase signals, characteristic data for an SMM, and an Arrhenius plot of the relaxation time gave a re-orientation energy barrier (ΔE) of 18.1 K and a pre-exponential factor of 1.63×10^{-7} s. Magnetization experiments on aligned single crystals below 0.7 K showed a stepped hysteresis loop, confirming the occurrence of quantum tunneling of the on magnetization (QTM). QTM was, on the other hand, suppressed by rapid sweeps of the magnetic field even at 0.5 K. The sweep-rate dependence of the spin flips can be understood by considering the Landau–Zener–Stückelberg (LZS) model.

Keywords: magnetic properties · manganese · mixed-valent compounds

Introduction

Nano-sized magnetic materials have attracted an increasing interest from the view points of quantum behavior[1] and their possible application to quantum devices.[2] High-spin molecules with easy-axis-type anisotropy show very slow thermal relaxation of the magnetization at very low temperatures and behave as single-domain magnets, classified as single-molecule magnets (SMMs).[3] SMMs undergo spin reorientation not only by thermal, but also by quantum processes. When spin sublevels in the spin ground state (described by $|S,M_s\rangle$) have the same energy under a field sweep, the two wave functions admix to form a tunneling gap (Δ). At a low enough temperature, the spin flips by means of an adiabatic process at the anticrossing point of spin sublevels, called quantum tunneling of the magnetization (QTM) (Figure 1a).[4] Amongst other selection rules for QTM, it is noted that a molecule with a half-integer spin quantum number does not show QTM at zero magnetic

[a] S. Koizumi, Dr. M. Nihei, Dr. T. Shiga, Prof. H. Oshio
Graduate School of Pure and Applied Sciences
Department of Chemistry University of Tsukuba
Tennodai 1-1-1, Tsukuba 305-8571 (Japan)
Fax: (+81) 29-853-4238
E-mail: oshio@chem.tsukuba.ac.jp

[b] Dr. M. Nakano
Department of Applied Chemistry
Graduate School of Engineering, Osaka University
2-1 Yamada-oka, Suita, Osaka 565-0871 (Japan)

[c] Prof. H. Nojiri
Institute of Material Research, Tohoku University
Katahira 2-1-1, Aoba-ku, Sendai 980–8577 (Japan)

[d] Dr. R. Bircher, Dr. O. Waldmann, Dr. S. T. Ochsenbein, Prof. H. U. Güdel
Department of Chemistry and Biochemistry
University of Bern, 3012 Bern, (Switzerland)

[e] Dr. F. Fernandez-Alonso
ISIS Facility, Rutherford Appleton Laboratory
Chilton, Didcot OX11 0QX, (United Kingdom)

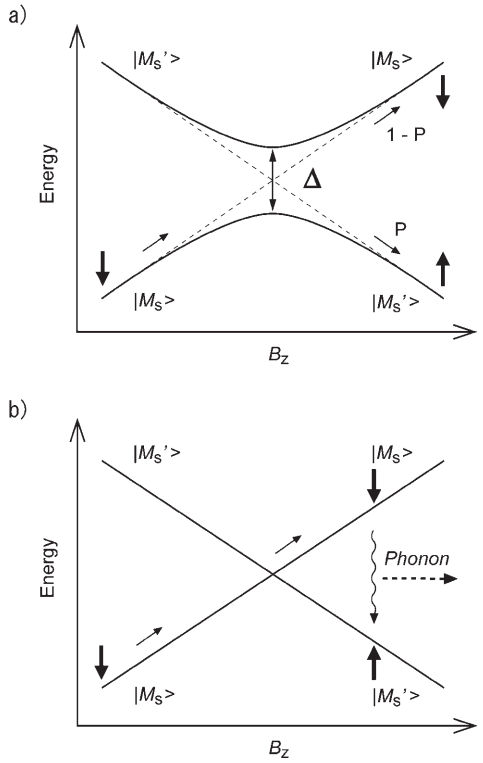

Figure 1. Spin reversal by a) adiabatic and b) non-adiabatic (thermal) processes. Δ and P denote the tunneling gap and tunneling probability, respectively.

field because of Kramers degeneracy. QTM was first observed in a dodecanuclear manganese cluster ($[Mn_{12}]$), which showed hysteresis loops with steps at constant intervals of magnetic field.[5] In QTM, the tunneling probability (P) between $|S,M_s\rangle$ and $|S,M_s'\rangle$ states is given by the Landau–Zener–Stückelberg (LZS) model, Equation (1),[6] in which dB/dt is the sweep rate of magnetic field.

$$P = 1-\exp\left[-\pi\Delta^2/(2\hbar g\mu_B|M_S-M_S'|dB/dt)\right] \quad (1)$$

The LZS model indicates that a slower sweep rate and/or larger tunneling gap enhances the tunneling probability. It is noted that, in an adiabatic process, the magnetic field of each QTM step is independent of the sweep rate.[3] The spin can also flip by a thermal (nonadiabatic) process, for which the reversal field depends on the sweep rate of the external magnetic field (Figure 1b). Magnetic measurements at sub-Kelvin temperature with variable field-sweep rates are, therefore, very useful to study the dynamics of the QTM. The micro-SQUID technique has been applied to study the quantum magnetic behavior of SMMs,[7] and other measurements, such as solid-state NMR and magnetic torque measurements, have been used for detailed studies of the $[Mn_{12}]$ and $[Fe_8]$ families. Studies on SMMs with different size, shape, and spin topology should provide a better understanding of the mechanism. Although many SMMs have been reported, the number of ring and wheel SMMs is still limited,[8] and more examples are hence desirable for understanding and exploiting the quantum phenomena characteristic of cyclic compounds. We report here the synthesis and magnetic properties of a novel mixed-valance manganese wheel SMM, $[Mn^{II}_3Mn^{III}_4(5\text{-}NO_2\text{-hbide})_6]\cdot 5C_2H_4Cl_2$ (**1**) ($H_3(5\text{-}NO_2\text{-hbide}) = N$-(2-hydroxy-5-nitrobenzyl)iminodiethanol). Magnetization experiments with different field scan rates are presented, and the quantum spin dynamics at very low temperatures are discussed. A part of this work has previously been reported as a communication.[9]

Results and Discussion

Structural description: Complex **1** crystallizes in the monoclinic space group $C2/c$, and the complex molecule is located on a crystallographic center of symmetry (Figure 2). Selected bond lengths and angles are listed in Table 1.

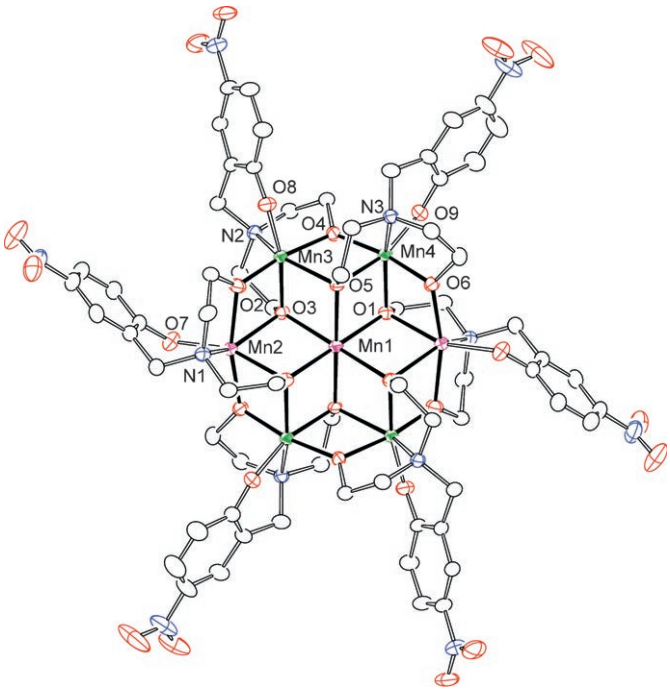

Figure 2. ORTEP diagram of a complex molecule **1** with 30% probability.

In **1**, seven manganese ions linked by six tri-anionic ligands form the wheel structure. Compound **1** is a neutral molecule, suggesting that the molecule has three Mn^{II} and four Mn^{III} ions. The oxidation states of the manganese ions can be assigned from charge considerations, coordination bond lengths, bond-valence-sum (BVS) calculations,[10] and the existence of Jahn–Teller distortions. BVS calculations yielded values of 2.01 and 2.26 for the three manganese ions (Mn1 and Mn2) and 3.22 and 3.20 for the other four manganese ions (Mn3 and Mn4), assuming Mn^{II} and Mn^{III}, respectively. On the bases of BVS calculations and the presence of

Table 1. Selected bond length [Å] and angles [°].[a]

Mn1–O1	2.168(6)	Mn1–O5	2.207(5)
Mn1–O3	2.212(5)	Mn2–O7	2.060(6)
Mn2–O6	2.094(6)	Mn2–O2	2.118(6)
Mn2–O1	2.213(5)	Mn2–O3*	2.259(6)
Mn2–N1	2.272(7)	Mn3–O2*	1.870(6)
Mn3–O8	1.873(6)	Mn3–O3	1.968(5)
Mn3–O4	1.979(6)	Mn3–N2	2.215(7)
Mn3–O5	2.251(5)	Mn4–O9	1.878(6)
Mn4–O6	1.903(5)	Mn4–O4	1.924(5)
Mn4–O5	2.015(6)	Mn4–O1	2.172(5)
Mn4–N3	2.254(7)		
Mn1-O1-Mn4	94.1(2)	Mn1-O1-Mn2	97.2(2)
Mn4-O1-Mn2	96.3(2)	Mn3*-O2-Mn2	109.3(3)
Mn3-O3-Mn1	102.9(2)	Mn3-O3-Mn2*	100.5(2)
Mn1-O3-Mn2*	94.6(2)	Mn4-O4-Mn3	111.1(3)
Mn4-O5-Mn1	97.5(2)	Mn4-O5-Mn3	97.8(2)
Mn1-O5-Mn3	94.49(19)	Mn4-O6-Mn2	109.5(3)

[a] Key to the symmetry operation; * $-x+1/2$, $-y+1/2$, $-z$.

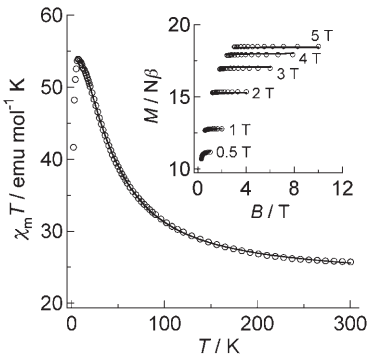

Figure 3. $\chi_m T$ versus T plot for **1**. The solid line was calculated using the parameters given in the text. Inset: Field dependence of the magnetization at 0.5–1.6 K with 0.5–5 T. The solid lines were calculated using the best-fit parameters of $S=19/2$, $g=2.00$, $D=-0.325$ K, and $B_4^0/k_B=-2.61\times10^{-5}$ K.

Jahn–Teller distortion in Mn^{III} ions, the two manganese ions on the rim (Mn2) and the one in the center (Mn1) are Mn^{II} ions, and the other four manganese ions (Mn3 and Mn4) are Mn^{III} ions. In the wheel, six μ_2-alkoxo groups (O2, O4, and O6) bridge the manganese ions on the rim, which themselves are linked to the central ion through six μ_3-groups (O1, O3, and O5) acting as spokes to form the wheel structure. The coordination geometry of the Mn^{II} ions (Mn1 and Mn2) is quasi-octahedral, and they have O_6 and N_1O_5 chromophores with bond lengths of 2.194(5)–2.211(5) Å and 2.048(5)–2.259(5) Å, respectively. The Mn^{III} ions (Mn3 and Mn4) have an axially elongated coordination geometry with the Jahn–Teller elongation axes along N2-Mn3-O5 and N3-Mn4-O1, respectively. Coordination bond lengths with axial atoms were 2.115(5)–2.239(6) Å, whereas the bond lengths involving the equatorial atoms are in the range of 1.859(5)–2.097(5) Å. In **1**, two symmetry-related molecules with *c*-glide reflection are tilted with an angle of 64.6°.

DC magnetic susceptibility: The temperature dependence of the magnetic susceptibility of a powder sample of **1** was measured in the temperature range of 1.8–300 K under an external magnetic field of 0.05 T (Figure 3). The $\chi_m T$ value of 25.71 emu mol^{-1} K at 300 K increased as the temperature was lowered, reaching a maximum value of 53.9 emu mol^{-1} K at 7.0 K. The sudden decrease in the $\chi_m T$ value below 7.0 K is due to the magnetic anisotropy and/or intermolecular antiferromagnetic interaction. The $\chi_m T$ value at 300 K is in agreement with the value expected for the noncorrelated three Mn^{II} and four Mn^{III} ions (25.125 emu mol^{-1} K, with $g=2.0$). The maximum $\chi_m T$ value at 7.0 K suggests that **1** has a relatively high spin ground states such as $S=21/2$ or 19/2, for which the calculated Curie constants are 60.375 or 49.875 emu mol^{-1} K, respectively, with $g=2.00$.

A modified vector-coupling model, for which the powder magnetic susceptibility data in the temperature range of 15–300 K were used and the contribution from the magnetic anisotropy and intermolecular magnetic interactions was neglected, was applied to estimate intramolecular exchange coupling constants. Three exchange parameters $J(Mn^{II},Mn^{II})$, $J(Mn^{II},Mn^{III})$, and $J(Mn^{III},Mn^{III})$ were supposed between the Mn^{II}–Mn^{II}, Mn^{II}–Mn^{III}, and Mn^{III}–Mn^{III} ions, respectively. Most of the interaction paths were taken into account by the use of a Kambe-type vector coupling scheme, and the redundant paths were compensated by using first-order perturbation terms. Nonlinear optimization converged to more than one set of model parameters: 1) $g=1.915$, $J(Mn^{II},Mn^{II})/k_B=6.29(3)$ K, $J(Mn^{II},Mn^{III})/k_B=0.831(3)$ K, and $J(Mn^{III},Mn^{III})/k_B=-2.322(8)$ K; 2) $g=1.904$, $J(Mn^{II},Mn^{II})/k_B=2.94(5)$ K, $J(Mn^{II},Mn^{III})/k_B=3.6(1)$ K, and $J(Mn^{III},Mn^{III})/k_B=-9.3(3)$ K; 3) $g=1.932$, $J(Mn^{II},Mn^{II})/k_B=3.81(3)$ K, $J(Mn^{II},Mn^{III})/k_B=2.018(9)$ K, and $J(Mn^{III},Mn^{III})/k_B=-5.61(2)$ K. These parameter sets gave a spin ground state of $S=19/2$, 17/2, and 19/2, respectively. The estimated g values were smaller than the average value expected for the three Mn^{II} and four Mn^{III} ions. Therefore, we analyzed the magnetic susceptibility data with the g value fixed to 2.0 and obtained two sets of parameters: 1) $J(Mn^{II},Mn^{II})/k_B=3.40(4)$ K, $J(Mn^{II},Mn^{III})/k_B=1.87(5)$ K, and $J(Mn^{III},Mn^{III})/k_B=-5.7(1)$ K and 2) $J(Mn^{II},Mn^{II})/k_B=5.1(1)$ K, $J(Mn^{II},Mn^{III})/k_B=0.68(4)$ K, and $J(Mn^{III},Mn^{III})/k_B=-2.3(1)$ K, giving a spin ground state of $S=17/2$ and 19/2, respectively. It should be noted that the analysis of the powder magnetization data (vide infra) yielded a g value of 2.000(3) for an $S=19/2$ ground state. Although it is difficult to extract a unique parameter set for a spin-frustrated system, such as **1**,[11] the consistency with other data suggests that a ground spin state of $S=19/2$ is most likely.[9] It should also be noted that an $S=19/2$ spin ground state cannot be described as a simple picture of up and down spin alignments, but as a non-collinear spin structure of tilted spins due to the spin frustration.

The magnetization data for a powdered sample of **1** were collected in the temperature range of 0.5–1.6 K and with a magnetic field of 0.5–5 T and they are plotted as reduced magnetization ($M/N\beta$) versus B/T in Figure 3 (inset). The data were used to estimate the ground spin state and the axial zero-field splitting parameter D and were analyzed by

assuming only the ground state is populated. The spin Hamiltonian [Eq. (2)] used included the isotropic Zeeman, axial ($D\hat{S}_z^2$)[12] and the higher order (B_4^0)[13] terms of the zero-field-splitting parameter.

$$\hat{\mathbf{H}} = g\mu_B \hat{H}\cdot\hat{S} + D[\hat{S}_z^2 - 1/3\,S(S+1)] + B_4^0\hat{\mathbf{O}}_4^0$$
$$\hat{\mathbf{O}}_4^0 = 35\,\hat{S}_z^4 - 30\,S(S+1)\hat{S}_z^2 + 25\,\hat{S}_z^2 + 6S(S+1) \qquad (2)$$

The best-fit parameters were obtained as $g=2.000(3)$, $D=-0.325(1)$ K, and $B_4^0/k_B=-2.61(1)\times10^{-5}$ K.

Single-crystal magnetization was also measured to confirm the spin ground state of the molecule (Figure 4). The X-ray

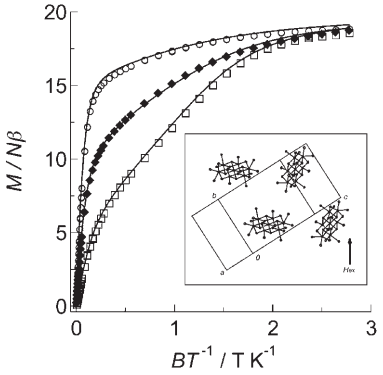

Figure 4. Field dependences of the magnetization at 1.8 K for **1**: (◆) powder sample, (○) parallel (on *bc* plane and normal to the (011) plane), and (□) perpendicular (parallel to *a* axis) magnetization for aligned single crystals for **1**. The solid lines were calculated using the parameters given in the text. Crystal packing diagram viewed on the *bc* plane (inset). The arrow denotes the external magnetic field (H_{ex}) direction for the parallel magnetization measurement on the aligned single crystals.

structure analysis showed that two symmetry-related molecules tilt 64.6° in relation to each other in the crystal (Figure 4, inset). An external magnetic field was applied normal to the (011) plane on the *bc* plane or parallel to crystallographic *a* axis. The perpendicular (*a* axis) and parallel (*bc* plane) magnetization data were reproducible with the parameters, $g=2.00$ (fixed), $D/k_B=-0.232(9)$ K, and $B_4^0/k_B=-3.3(3)\times10^{-5}$ K for a $S=19/2$ state, assuming that the principal axes of the two symmetry-related molecules are tilted by 0.0° and 54.2(7)°, respectively, to the external magnetic field. The estimated tilt angle was slightly different from the value of 64.6° obtained by the X-ray analysis.

High-field EPR measurements: HF-EPR spectra for microcrystalline samples of **1** were collected at several frequencies (125–190 GHz) and temperatures (4.2–60 K). The spectra at 190 GHz in the temperature range of 4.2–15 K are shown in Figure 5. In HF-EPR spectra the transitions between sublevels ($\Delta M_s=\pm1$) of the spin ground state can be directly observed as resonance absorption peaks. The relative intensities of the resonance peaks depend on the Boltzmann distribution among the sub levels in the spin ground state, which

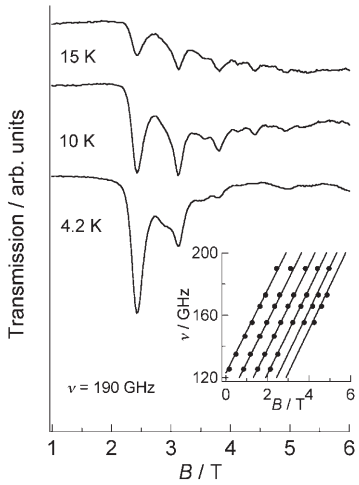

Figure 5. Quasi-single crystal HF-EPR spectra (190 GHz) for **1**. Microcrystalline samples were aligned by the strong external magnetic field. Inset: Microwave frequency versus resonance field for the peaks observed in the HF-EPR spectra. Solid lines result from a least-squares fit using the parameters described in the text. The applied magnetic field was revealed to have an angle of 15° with respect to the molecular easy axis.

helps to determine the sign of the *D* value. The spectrum at 4.2 K showed three resonance peaks at 2.44, 3.35, and 3.82 T. As the temperature was increased up to 15 K, new peaks appeared at 4.40 and 4.96 T. For a molecule with a negative *D* value, the EPR transitions at the lowest field become the most intense at lower temperatures, whereas the finer structures at the higher fields should be observed at higher temperatures. The temperature dependence of the observed HF-EPR spectra clearly indicates that **1** has a negative *D* value. The weak peaks at 2.90, 3.60, and 4.12 T might be due to transitions in excited states with different total spin.

The HF-EPR spectra were analyzed assuming 1) that the loosely packed polycrystalline sample was torqued in a strong magnetic field, such that most crystallites aligned their easy axes along the field and 2) that only the $S=19/2$ ground spin manifold was populated at the measurement temperatures. For the data analysis, we used the spin Hamiltonian [Eq. (2)], including the angle between the molecular easy axis and external magnetic field (θ). Nonlinear least-squares fitting of the resonance field data, incorporating the eigenfield method,[14] gave the spin Hamiltonian parameters of $g=2.00$ (fixed), $D/k_B=-0.283(1)$ K, $B_4^0/k_B=-1.64(1)\times10^{-5}$ K, and $\theta=15.1°$. Note that the precise direction of the principal axis of *D* cannot be determined uniquely from the molecular structure without extensive theoretical study, because of the low symmetry of the molecules. Simulation curves calculated with the best-fit parameters are presented in Figure 5 (inset), and the satisfactory agreement with the data confirms a rather narrow distribution of the crystalline alignments, that is, of essentially fully torqued polycrystallines. Considering the two symmetry-related molecules, angle θ in the high-field experiments is expected to be close

to the half of mutual angle of these molecules. From magnetization experiments, the twist angle of the easy axes for the symmetry-related molecules was estimated to be 54.2°, and this value was larger than the $2\theta = 30.2°$ obtained from the HF-EPR measurements. This discrepancy should be due to an uneven torque of crystal with a preferred direction. It is suggested that in the HF-EPR experiments one half of the molecules are aligned with their principle axis tilted by 15° to the external magnetic field. The other half molecules are likely lying on a near-equatorial plane, such that the stronger transverse field smeared out their EPR signals.

Inelastic neutron scattering (INS): Figure 6 (inset) shows the INS spectra of **1** measured at 1.5, 6, and 14 K, summed over all scattering angles. Positive and negative energy transfer corresponds to neutron energy loss and gain, respectively.

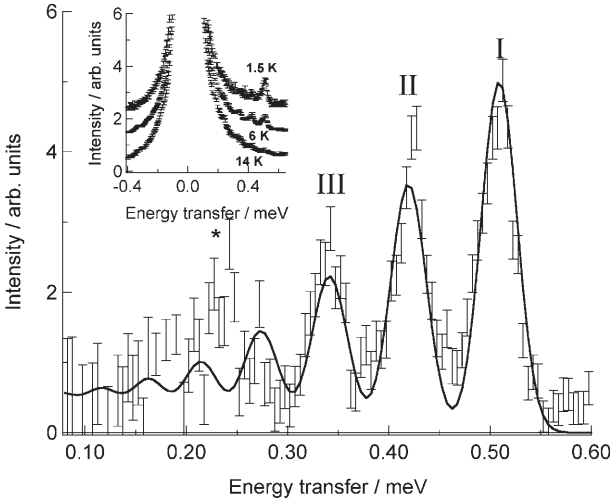

Figure 6. Inelastic neutron scattering (INS) spectra (inset) of **1** measured on IRIS with an analyzing energy of 1.84 meV at 1.5, 6, and 14 K (top to bottom, drawn with an offset), summed over all scattering angles. INS spectrum at 6 K corrected for contributions from the instrument and quasi-elastic scattering. I–III denote the observed peaks used for the data analysis. The solid line corresponds to the simulated INS spectrum as described in the text. The asterisk depicts a spurious contribution from fast neutrons.

The 1.6 K spectrum is dominated by an excitation at about 0.51 meV. The spectra measured at 6 K and 14 K exhibit a series of hot bands at lower energy transfers. On the neutron-energy-loss side of the 6 K spectrum, three almost equidistant peaks were clearly observed at about 0.34, 0.42, and 0.51 meV, whereas on the lower energy-transfer side, additional intensity was observed. The 14 K data did not show distinct peaks, because the magnetic intensity was distributed over many transitions. The INS spectrum at 6 K, after subtraction of a background accounting for the instrumental resolution function as well as quasi-elastic scattering processes, is shown in Figure 6. In the spectrum, there was a spurious feature due to fast neutrons (asterisk in Figure 6) that is not related to the sample. Three well-resolved peaks were used in the data analysis. The exact peak positions were determined by fits of single Gaussians to the corrected data, which gave 0.338(4), 0.423(4), and 0.507(3) meV.

Assuming a well-isolated ground state, the giant-spin model equation [Eq. (2)] can be used again to describe the INS spectra of **1** (if the magnetic field is set to zero). Inclusion of an E term turned out to be unnecessary in the data analysis. The D term in Equation (2) splits a half-integer ground state into $(2S+1)/2$ Kramer doublets, with the $M_S = \pm S$ doublet lying lowest in energy for $D < 0$. For an $S = 19/2$ spin ground state nine INS transitions are predicted by the selection rule $\Delta M_S = \pm 1$. The relative INS intensities I_{nm} of these transitions can be approximated by Equation (3),[15] in which S^+ and S^- are the spin raising and lowering operators, respectively.

$$I_{nm} \propto (2|\langle\psi_n|\hat{S}_z|\psi_m\rangle|^2 + |\langle\psi_n|\hat{S}^+|\psi_m\rangle|^2 + |\langle\psi_n|\hat{S}^-|\psi_m\rangle|^2) \qquad (3)$$

Least-squares fits of the transition energies calculated from Equation (3) to the three well-resolved experimental peaks yielded the zero-field-splitting parameters of $D = -0.274(7)$ K and $B_4^0 = -2.1(9) \times 10^{-5}$ K. The calculated peak positions of 0.341, 0.419, and 0.509 meV agreed with the experimental peak positions, and the deviations were within experimental error. The calculated spectrum depicted in Figure 6 also reproduced the intensities well. Deviations only occur at lower energy transfers, at which the experimental data do not allow for a precise peak location.

AC magnetic susceptibility: Complex **1** possesses an $S = 19/2$ spin ground state and negative D value; therefore, **1** is thought to be an SMM and should show slow magnetic relaxation at low temperature. Evidence for slow relaxation of magnetization in **1** was obtained by AC magnetic susceptibility measurements. AC magnetic susceptibility measurements for polycrystalline sample were performed in the temperature range of 1.8–4.0 K with an AC field of 3 G oscillating at 10–1000 Hz. Complex **1** gave frequency-dependent in-phase (χ') and out-of-phase (χ'') signals, the peak maxima of which shifted to lower temperatures as the AC frequency decreased (Figure 7). The AC magnetic susceptibility data confirm that **1** is an SMM. Assuming that the relaxation time (τ) at the peak-top temperature of χ'' is well approximated by the inverse of the AC frequency, the Arrhenius plot gave an effective energy barrier for magnetization reversal (ΔE_{eff}) of 18.1 K and a pre-exponential factor of $\tau_0 = 1.63 \times 10^{-7}$ s (Figure 7b inset).

Single-crystal magnetization experiments under a static field: Observation of a magnetic hysteresis without long-range order under application of a longitudinal magnetic field is direct evidence for an SMM. Magnetic hysteresis measurements on aligned single crystals were carried out in the temperature range of 500–1070 mK, during which the external magnetic field was applied parallel to the crystallographic a axis, with a very slow field-sweep rate of $\approx 10^{-4}$ T s^{-1}. Because the two molecular sites in a crystal are

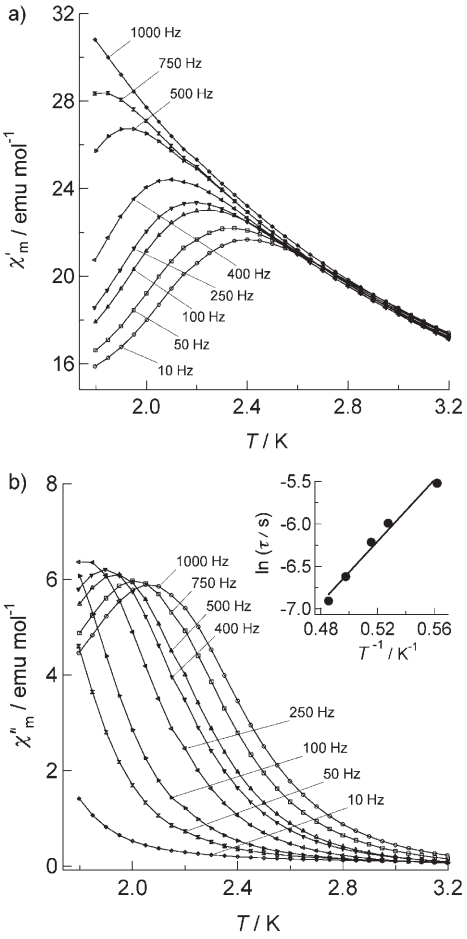

Figure 7. Temperature dependences of a) in-phase (χ'_m) and b) out-of-phase (χ''_m) signals of the AC magnetic susceptibility measurements in oscillating field of 3 G, and the natural logarithm of the relaxation time (τ) versus the inverse of the temperature plot for **1**.

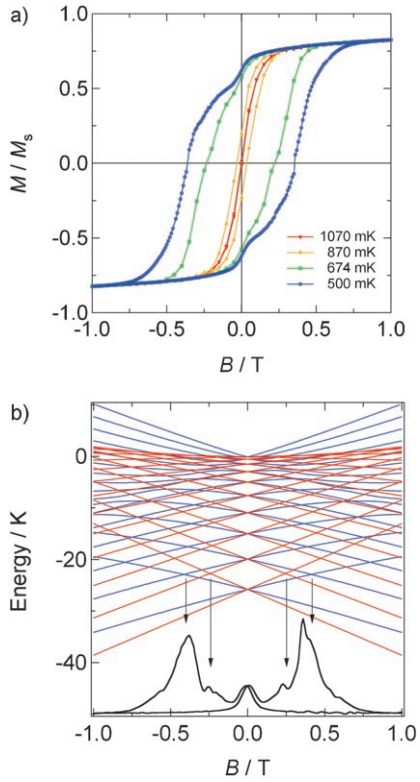

Figure 8. a) Magnetic hysteresis loops for aligned single crystals of **1** under static field in the temperature range from 1070–500 mK. The applied DC field was perpendicular to the wheel plane of one of the two crystallographically related molecules. b) A plot (black line) of the derivative of the magnetic moment (dM/dB) versus magnetic field at 500 mK, and Zeeman splitting diagrams for $S=19/2$, $g=2.000$, $D=-0.25$ K, and $B_4^0=-2.61\times10^{-5}$ K with magnetic fields parallel to (red lines) and tilted (blue lines) by 53.74° from the principal axis of the molecule.

related by a *c*-glide operation, one half of the molecules have their easy axes in the direction of the external field ($\theta=0°$), whereas the remaining half has the easy axes canted by $\approx53°$ from the field direction *a*. The results are depicted in Figure 8a.

Magnetic hysteresis loops are evident below 870 mK; the coercivities increased upon decreasing the temperature. The hysteresis loop at 500 mK clearly showed the step-like features indicative of QTM. The derivative of the magnetic moment (dM/dB) at 500 mK is plotted versus magnetic field in Figure 8b. The derivative curves showed three major peaks at 0 and ±0.40 T and small peaks at ±0.24 T. The field positions of the peaks at 0 and ±0.24 T agree with the calculated level-crossing fields of the spin sublevels ($M_s=+19/2$ and $-19/2$ at 0 T, $M_s=+19/2$ and $-17/2$ at $+0.24$ T, and $M_s=-19/2$ and $+17/2$ at -0.24 T, respectively) further indicating QTM. The broad peaks at around ±0.40 T can be attributed to the QTM of the molecules tilted by $\approx53°$, taking into account that the longitudinal magnetic field for these molecules was reduced by the tilting according to the level-crossing condition $B_{ext}\cos\theta=\pm0.24$ T (θ is the angle of the magnetic field to the principal axis of the molecule). Zeeman splitting diagrams ($\theta=0°$ and 53°) calculated by using the parameters for the $S=19/2$ state together with observed data are shown in Figure 8b. There were some shoulder peaks in the dM/dB plot, for which the peak positions did not correspond to the level-crossing fields of the spin sublevels. This might be due to misalignment of the single crystals. It is noted that **1** shows QTM in zero external magnetic field in spite of the half-integer spin ground state of the molecule. According to Kramers' theorem, half-integer spin systems have degenerate $\pm M_s$ sublevels in zero magnetic field,[16] and no QTM should be observed due to the absence of a tunneling gap. However, external perturbations, such as nuclear hyperfine fields and/or dipolar fields, can remove the degeneracy of the sublevels,[17] and QTM becomes possible even at zero field. This effect has been observed in the half-integer spin systems such as $[PPh_4][Mn_{12}O_{12}(O_2CEt)_{16}(H_2O)_4]$[18] ($S=19/2$) and $[Mn_4O_3(OSiMe_3)OAc_3(dbm)_3]$ ($S=9/2$) (dbm = dibenzoylmethane).[19]

Single-crystal magnetization experiments under pulse field: The probability of QTM at a two-level crossing depends on

the tunneling gap (Δ), the difference of magnetic quantum number ($\Delta M_s = M_s - M_s'$), and the field-sweep rate (dB/dt), as predicted by the LZS model [Eq. (1)]. To examine the sweep rate dependence of the QTM, we used a pulse magnet for the magnetic hysteresis measurements.

The external field was swept with a rate of $\approx 10^3\,T\,s^{-1}$, starting from 0 T up to a maximum field of $+B_p$, and then reversed down to $-B_p$. The exact values of the sweep rate depend on the field range $\pm B_p$ of the pulsed field, and are roughly proportional to B_p^{-1}. Magnetization curves were collected for the aligned single crystals of **1**, in a similar way as for the slow passage experiments, with the applied magnetic field ranging from $B_p = 0.3$ to 5 T at 500 mK. Selected magnetization curves (M) and their derivatives (dM/dB) are plotted versus magnetic field (B) in Figure 9. For magnetic

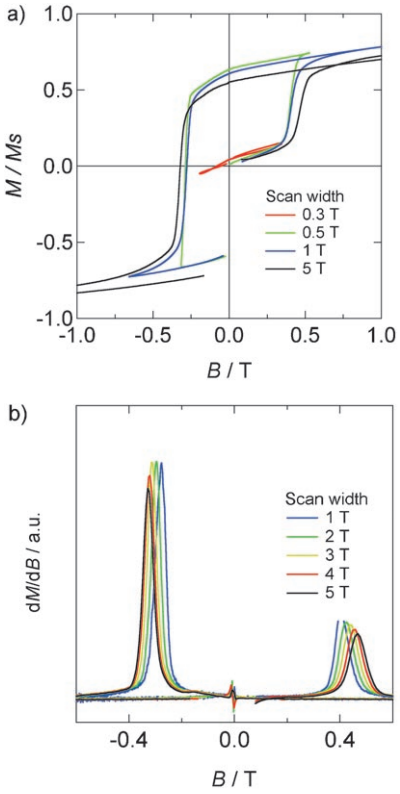

Figure 9. a) Magnetization curves (M) and b) field derivatives (dM/dB) versus B for various scan widths of the pulsed magnetic field at 0.5 K for aligned single crystals of **1**. Field was applied as in as the static-field experiments.

fields up to $B_p = 0.3$ T, which is just above the first level-crossing field of the $\theta = 0°$ species and below the level-crossing field of the $\theta \approx 53°$ species, no magnetization jumps were observed. In the zero field, the ground sublevels $M_s = \pm 19/2$ are equally populated for zero-field cooled sample, yielding zero net magnetization of the sample. If the field is then swept rapidly enough, the population of the spin sublevels does not attain thermal equilibrium, and the net moment shows a linear dependence on the magnetic field, which is attributable to a transverse magnetization from the canted molecules ($\theta \approx 53°$). At faster filed-sweep rates (or $B_p = 0.5$ T), magnetization jumps similar to the ones found in the slow passage experiments were observed, either at around $+0.4$ T for increasing field ($0 \rightarrow +B_p$) or at -0.3 T for decreasing field ($+B_p \rightarrow -B_p$). The peaks in dM/dB showed a dependence of the sweep rate, that is, they moved to larger fields as the sweep rate became faster. Apparently, such peak shifts, characteristic of kinetic retardation, seem to be inconsistent with a pure QTM process. Nevertheless, such kinetic effects on tunneling processes have been reported for the Landau–Zener model coupled to a phonon bath.[20] Coupling between a tunneling center and a heat bath allows energy exchange, causing kinetic effects. Therefore, it was concluded that the magnetization jumps observed in the pulsed experiments correspond to that found in the slow passage experiments, and are interpreted as the (adiabatic) QTM process of the $\theta \approx 53°$ species from the $M_s = \pm 19/2$ to the $M_s = \pm 17/2$ sublevels. In the pulsed magnetic field experiments, QTM of the $\theta = 0°$ species at the level-crossing fields 0 and ± 0.24 T was not observed, in contrast to the slow passage experiments. This is likely due to the absence of a transverse magnetic field, which could enhance really small tunneling matrix elements of the $\theta = 0°$ species for very fast field sweep rates. It is also noted that the hysteresis curves in the pulsed field experiments were asymmetric. As shown in Figure 9b, the peaks in dM/dB are broader for the rising edges than that for the falling edges, in addition to the different peak fields for the two edges. These observations can be explained by an "exchange bias" from neighboring molecules.[21] In the initial stage ($0 \rightarrow +B_p$), the sample is not magnetized at first, and the effect of a mean-field bias is negligible. On the other hand, the sample is fully magnetized in the falling stage ($+B_p \rightarrow -B_p$), with a magnetization $M \approx +N\mu_B S$ antiparallel to the external field $-B_p$, which imposes a mean-field bias enhancing the external field through antiferromagnetic intermolecular interactions. Thus, the bias field from the surrounding molecules shifts the level-crossing fields as compared to the values for a bare molecule. The estimated bias of ≈ 0.1 T corresponds to the value expected for an intermolecular exchange interaction of $|zJ|/k_B \approx 0.7 \times 10^{-3}$ K. It is known that the distribution of internal fields is smaller near saturation of magnetization than in a sample of zero net magnetization. The different broadness in dM/dB for the rising and the falling edges likely reflect the fluctuations in the internal field.[22]

Conclusion

A heptanuclear $Mn^{II,III}$ wheel SMM was synthesized and characterized. Detailed analyses of the magnetic, HF-EPR data for aligned single crystals, and inelastic neutron scattering (INS) data suggests that the molecule has an $S = 19/2$ spin ground state with an easy-axis-type magnetic anisotropy of $D = -0.283$ K. Magnetization experiments with static and pulsed field magnets showed different magnetic hysteresis

loops. For a static field, the spin reversal at 0.5 K was governed by an adiabatic process, whereas for a pulsed field the QTM at 0 T was suppressed owing to the small tunneling probability and fast field-sweep rate.

Experimental Section

Synthesis: All reagents were obtained from commercial suppliers and were used without further purification. The ligand H_3(5-NO_2-hbide) (*N*-(2-hydroxy-5-nitrobenzyl)iminodiethanol) was prepared by the literature method.[23]

$[Mn^{II}_3Mn^{III}_4$(5-NO_2-hbide)$_6]\cdot 5C_2H_4Cl_2$ (1): $Mn(OAc)_2\cdot 4H_2O$ (246 mg, 1 mmol) in methanol (10 mL) was added to the mixture of H_3(5-NO_2-hbide) (256 mg, 1 mmol) and triethylamine (303 mg, 3 mmol) in methanol (20 mL), and a brown precipitate formed immediately. The brown precipitate (15 mg) was dissolved in 1,2-dichloroethane (50 mL), and after standing for a week stand dark brown lozenge and hexagon plates crystals of **1** (60 %), which had five and seven solvent molecules, respectively, were obtained. The molecular structures in the penta- and hepta-solvated crystals were identical, but had different packing structures. Complex **1** with five dichloromethane had a more parallel molecular alignment and was used for single-crystal magnetic measurements. elemental analysis calcd (%) for dried **1** ($C_{66}H_{78}Mn_7N_5O_{30}$): C 41.64, H 4.13, N 8.83; found: C 41.80, H 4.56, N 8.57.

Crystal structure analysis: A single crystal of **1** was mounted with epoxy resin on the tip on a glass fiber. Diffraction data were collected at 200 K using a Bruker SMART APEX diffractometer equipped with a CCD-type area detector. A full sphere of data was collected with graphite-monochromated $Mo_{K\alpha}$ radiation ($\lambda = 0.71073$ Å). At the end of data collection, the first 50 frames of data were recollected to establish that the crystal had not deteriorated during the data collection. The data frames were integrated using the SAINT program and merged to give a unique data set for structure determination. Absorption correction by integration was applied on the basis of measured indexed crystal faces using XPREP. The structure was solved by the direct method and refined by the full-matrix least-squares methods on all F^2 data using the SHELXTL 5.1 package (Bruker Analytical X-ray Systems). Non-hydrogen atoms were refined with anisotropic thermal parameters. Hydrogen atoms were included in calculated positions and refined with isotropic thermal parameters riding on those of the parent atoms. Crystal data are reported in Table 2. CCDC-646168 contains the supplementary crystallographic data for this paper. These data can be obtained free of charge from The Cambridge Crystallographic Data Centre via www.ccdc.cam.ac.uk/data_request/cif.

Physical measurements: Magnetic susceptibility data with an applied magnetic field of 500 G were obtained by on a MPMS SQUID magnetometer (Quantum Design). Magnetization data down to 0.5 K were collected with the same magnetometer equipped with a self-built ^{3}He cryostat (i-Quantum). AC magnetic susceptibility was measured at frequencies from 10 to 1000 Hz with an AC field amplitude of 3 G; no DC field was applied. Diamagnetic corrections were done by using Pascal's constants.[24] Single crystals aligned by hand were used for magnetic susceptibility and magnetization measurements. High-field EPR (HF-EPR) spectra were measured by using a simple transmission method with Gunn oscillators as radiation source for 125–190 GHz, an InSb bolometer as a detector, and a homemade HF-EPR spectrometer with TESRA-IMR was used.[25] Inelastic neutron scattering (INS) measurements were performed on the inverted geometry time-of-flight spectrometer (IRIS) at the pulsed neutron spallation source IRIS at the Rutherford Appleton Laboratory (UK), with a PG002 graphite analyzer with an analyzing energy of 1.84 meV. Data were collected at three temperatures (1.5, 6, and 14 K) and corrected for detector efficiency by means of a vanadium reference. The resolution of the instrument at the elastic position was 18 μeV, and a momentum transfer range (Q) was 0.3–1.8 Å^{-1}. A fresh sample of 2 g of undeuterated **1** was placed under helium in an aluminum hollow cylinder can with an outer diameter of 23 mm and a sample thickness of 2 mm.

Table 2. Crystallographic data for **1**.

formula	$C_{76}H_{98}Cl_{10}Mn_7N_{12}O_{30}$
M_w	2398.75
crystal system	monoclinic
space group	*C*2/*c*
a [Å]	34.133(5)
b [Å]	13.521(2)
c [Å]	21.959(3)
β [°]	104.721(3)
V [Å^3]	9802(3) Å^3
Z	4
T [K]	200
ρ_{calcd} [g cm^{-3}]	1.612
μ [mm^{-1}]	1.271
F(000)	4812
crystal size [mm^3]	0.30×0.10×0.10
θ range [°]	$1.81 \le \theta \le 23.29$
reflections collected	22177
independent reflections	7066 [$R_{int} = 0.1123$]
max/min transmission	0.887/0.710
GOF on F^2	1.047
final *R* indices [$I > 2\sigma(I)$]	$R1 = 0.0869$, $wR2 = 0.1769$
R indices (all data)	$R1 = 0.1505$, $wR2 = 0.2049$
largest diff. peak/hole [e Å^{-3}]	0.598/−0.692

The container was inserted in a standard ILL orange cryostat. Magnetization measurements under pulsed field were performed by means of a standard inductive method. A home made high-field system with a variable sweep rate was combined with a capacitor bank described elsewhere.[26] The apparatus with the pulsed magnetic field generator provided field rates up to 10^3 T/sec and was equipped with a ^{3}He refrigerator. The sample was immersed directly in the liquid ^{3}He. The sample temperature was kept constant during the field pulse.

Acknowledgements

This work was partially supported by a Grant-in-Aid for Scientific Research from the Ministry of Education, Culture, Sports, Science and Technology (Japan), and by TARA projects of University of Tsukuba.

[1] a) S. Kubatkin, A. Danilov, M. Hjot, J. Cornil, J.-L. Brédas, N. Sthuhr-Hassen, P. Hedegård, T. Bjørnholm, *Nature* **2003**, *425*, 698; b) A. S. Majetich, Y. Jin, *Science* **1999**, *284*, 470; c) C. B. Murray, C. R. Kagan, M. G. Bawendi, *Science* **1995**, *270*, 1335; d) A. J. Zarur, J. Y. Ying, *Nature* **2000**, *403*, 65.

[2] a) J. A. Jones, *Science* **1998**, *280*, 229; b) M. N. Leuenberger, D. Loss, *Nature* **2001**, *410*, 789; c) W. Wernsdorfer, R. Sessoli, *Science* **1999**, *284*, 133.

[3] a) G. Aromi, S. M. J. Aubin, M. A. Bolcar, G. Christou, H. J. Eppley, K. Folting, D. N. Hendrickson, J. C. Huffman, R. C. Squire, H.-L. Tsai, S. Wang, M. W. Wemple, *Polyhedron* **1998**, *17*, 3005; b) D. Gatteschi, R. Sessoli, *Angew. Chem.* **2003**, *115*, 278; *Angew. Chem. Int. Ed.* **2003**, *42*, 268; c) H. Oshio, M. Nakano, *Chem. Eur. J.* **2005**, *11*, 5178; d) H. Oshio, N. Hoshino, T. Ito, M. Nakano, *J. Am. Chem. Soc.* **2004**, *126*, 8805; e) H. Oshio, M. Nihei, A. Yoshida, H. Nojiri, M. Nakano, A. Yamaguchi, Y. Karaki, H. Ishimoto, *Chem. Eur. J.* **2005**, *11*, 843.

[4] a) D. Gatteschi, A. Caneschi, L. Pardi, R. Sessoli, *Science* **1994**, *265*, 1054; b) A. Müller, F. Peters, M. T. Pope, D. Gatteschi, *Chem. Rev.* **1998**, *98*, 239.

[5] a) L. Thomas, F. Lionti, R. Ballou, D. Gatteschi, R. Sessoli, B. Barbara, *Nature* **1996**, *383*, 145; b) R. Sessoli, D. Gatteschi, A. Caneschi, M. A. Novak, *Nature* **1993**, *365*, 141; c) R. Sessoli, H.-L. Tsai, A. R.

Schake, S. Wang, J. B. Vincent, K. Folting, D. Gatteschi, G. Christou, D. N. Hendrickson, *J. Am. Chem. Soc.* **1993**, *115*, 1804.
[6] a) L. Landau, *Phys. Z. Sowjetunion* **1932**, *4*, 46; b) C. Zener, *Proc. R. Soc. London Ser. A* **1932**, *137*, 696; c) E. C. G. Stückelberg, *Helv. Phys. Acta* **1932**, *5*, 369.
[7] a) W. Wernsdorfer, R. Sessoli, D. Gatteschi, *Europhys. Lett.* **1999**, *47*, 254; b) W. Wernsdorfer, *Adv. Chem. Phys.* **2001**, *118*, 99.
[8] a) A. J. Tsaiopoulos, A. Vinslava, W. Wernsdorfer, K. A. Abboud, G. Christou, *Angew. Chem.* **2004**, *116*, 2169; *Angew. Chem. Int. Ed.* **2004**, *43*, 2117; b) C. Cadiou, M. Merrie, C. Paulsen, V. Villar, W. Wernsdorfer R. E. P. Winpenny, *Chem. Commun.* **2001**, 2666; c) R. W. Saarfrank, A. Scheurer, R. Prakash, F. W. Heinemann, T. Nakajima, F. Hampel, R. Leppin, B. Piawa, H. Rupp, P. Müller, *Inorg. Chem.* **2007**, *46*, 1586.
[9] S. Koizumi, M. Nihei, M. Nakano, H. Oshio, *Inorg. Chem.* **2005**, *44*, 1208.
[10] a) I. Brown, D. Altermatt, *Acta Crystallogr. Sect. B* **1985**, *41*, 244; b) W. Liu, H. H. Thorp, *Inorg. Chem.* **1993**, *32*, 4102.
[11] G. L. Abbati, A. Cornia, A. C. Fabretti, A. Caneschi, D. Gatteschi, *Inorg. Chem.* **1998**, *37*, 3759.
[12] a) G. Aromi, M. J. Knapp, J.-O Claude, J. C. Huffman. D. N. Hendrickson, G. Christou, *J. Am. Chem. Soc.* **1999**, *121*, 5489; b) H. J. Eppley, H.-L. Tsai, N. de Vries, K. Folting, G. Christou. D. N. Hendrickson, *J. Am. Chem. Soc.* **1995**, *117*, 301.
[13] a) A. L. Barra, D. Gatteschi, R. Sessoli, *Phys. Rev. B* **1997**, *56*, 8192; b) S. M. J. Aubin, N. R. Dilley, L. Pardi, J. Krzystek, M. W. Wemple, L.-C. Brunel, M. B. Maple, G. Christou, D. N. Hendrickson, *J. Am. Chem. Soc.* **1998**, *120*, 4991.
[14] B. B. Belford, R. L. Belford, J. F. Burkhalter, *J. Magn. Reson.* **1973**, *11*, 251.
[15] a) R. J. Birgenau, *J. Phys. Chem. Solids* **1972**, *33*, 59; b) O. Waldmann, H. U. Güdel, *Phys. Rev. B* **2005**, *72*, 094422.
[16] a) H. A. Kramers, *Proc. R. Acad. Sci. Amsterdam* **1930**, *33*, 959; b) L. Landau, E. M. Lifschitz, *Quantum Mechanics*, Pergamom, London, **1959**.
[17] a) V. N. Prokofcev, P. C. E. Stamp, *Phys. Rev. Lett.* **1998**, *80*, 5794; b) V. N. Prokofcev, P. C. E. Stamp, *J. Low Temp. Phys.* **1996**, *104*,143.
[18] S. M. J. Aubin, S. Spagna, H. J. Eooley, R. D. Sager, G. Christou, D. N. Hendrickson, *Chem. Commun.* **1998**, 803.
[19] W. Wernsdorfer, S. Bhaduri, C. Boskovic, G. Christou, D. N. Hendrickson, *Phys. Rev. B* **2002**, *65*, 180403.
[20] a) Y. Kayanuma, H. Nakayama, *Phys. Rev. B* **1998**, *57*, 13099; b) S. Miyashita, K. Saito, H. Nakano, M. Nishino, *Prog. Theor. Phys. Suppl.* **2002**, *145*, 370.
[21] a) R. Tiron, W. Wernsdorfer, N. Aliaga-Alcalde, G. Christou, *Phys. Rev. B* **2003**, *68*, 140407(R); b) E.-C. Yang, W. Wernsdorfer, S. Hill, R. S. Edwards, M. Nakano, S. Maccagnano, L. N. Zakharov, A. L. Rheingold, G. Christou, D. N. Hendrickson, *Polyhedron* **2003**, *22*, 1727; c) W. Wernsdorfer, S. Bhaduri, A. Vinslava, G. Christou, *Phys. Rev. B* **2005**, *72*, 214429.
[22] a) T. Ohm, C. Sangregorio, C. Paulsen, *Eur. Phys. J. B* **1998**, *6*, 195; b) B. Parks, J. Loomis, E. Rumberger, D. N. Hendrickson, G. Christou, *Phys. Rev. B* **2001**, *64*, 184426.
[23] D. C. Crans, I. Boukhobza, *J. Am. Chem. Soc.* **1998**, *120*, 8069.
[24] W. E. Hatfield, *Theory and Application of Molecular Paramagnetism*; E. A. Boudreaux, L. N. Mulay, Eds.; Wiley: New York, **1976**.
[25] H. Nojiri. A. Ajiro, T. Asano, J.-P Boucher, *New J. Phys.* **2006**, *8*, 218.
[26] a) K. Nakao, T. Atake, M. Wada, S. Takeyama, T. Sakakibara, N. Miura, *J. Phys. E* **1985**, *18*, 1018; b) N. Miura, *Physica B* **1994**, *201*, 40.

Received: May 10, 2007
Published online: August 29, 2007

